



### **Science Arts & Métiers (SAM)**

is an open access repository that collects the work of Arts et Métiers Institute of Technology researchers and makes it freely available over the web where possible.

This is an author-deposited version published in: <https://sam.ensam.eu>  
Handle ID: [.http://hdl.handle.net/10985/21360](http://hdl.handle.net/10985/21360)

#### **To cite this version :**

Martin BOURHIS, Michaël PEREIRA, Ivan DOBREV, Florent RAVELET - Innovative design method and experimental investigation of a small-scale and very low tip-speed ratio wind turbine - Experimental Thermal and Fluid Science - Vol. 130, p.110504 - 2021

Any correspondence concerning this service should be sent to the repository

Administrator : [scienceouverte@ensam.eu](mailto:scienceouverte@ensam.eu)



# Innovative design method and experimental investigation of a small-scale and very low tip-speed ratio wind turbine

M. Bourhis\*, M. Pereira, F. Ravelet, I. Dobrev

Arts et Metiers Institute of Technology, CNAM, LIFSE, HESAM University, 75013 Paris, France

## Keywords:

Small wind turbine  
Wind turbine design method  
Low tip-speed ratio  
Power and torque coefficients  
Stereoscopic particle image velocimetry

## ABSTRACT

Small horizontal axis wind turbines operating at low wind speeds face the issue of low performance compared to large wind turbines. A high amount of torque is required to start producing power at low wind speed to overcome friction of mechanical parts. A low design tip-speed ratio ( $\lambda$ ) is suitable for low power applications. The relevance of the classical blade-element/ momentum theory, traditionally used for the design of large wind turbines operating at high tip-speed ratio, is controversial at low tip-speed ratio. This paper presents a new design methodology for a 300 mm horizontal axis wind turbine operating at very low tip-speed ratio. Chord and blade angle distributions were computed by applying the Euler's turbomachinery theorem. The new wind turbine has multiple fan-type blades and a high solidity. The rotor was tested in wind tunnel. The power and torque coefficients have been measured, and the velocities in the wake have been explored by stereoscopic particle image velocimetry. The results are compared to a conventional 3-bladed horizontal axis wind turbine operating at higher tip-speed ratio  $\lambda = 3$ . The new wind turbine achieves a maximum power coefficient of 0.31 for  $\lambda = 1$ . The conventional wind turbine achieves similar performance. At low tip-speed ratio, the torque coefficient ( $C_t$ ) is higher for the new wind turbine than for the conventional one and decreases linearly with the tip-speed ratio. The high magnitude of torque at low tip-speed ratio allows it to have lower instantaneous cut-in wind speed ( $2.4 \text{ m}\cdot\text{s}^{-1}$ ) than the conventional wind turbine ( $7.9 \text{ m}\cdot\text{s}^{-1}$ ). The order of magnitude of the axial and tangential velocities in the near wake are closed to the design requirements. The current method could still be improved in order to better predict the profiles. The analysis of the wake shows that the new wind turbine induces a highly stable and rotating wake, with lower wake expansion and deceleration than the conventional one. This could be useful to drive a contra-rotating rotor.

## 1. Introduction

Wind is an inexhaustible resource. The conversion of the kinetic energy of the wind into mechanical or electrical energy useful for human activities has long been a source of concern. In fact, the first known wind power machine, a panemone windmill, was built in Persia from the 7th century for pumping water and grinding grain. Nowadays, academic research and engineering have made possible the industrialization of large wind turbines able to generate several megawatts. Various classifications of horizontal axis wind turbines are given in the literature [1,2] but few are sufficiently accurate at small scale. A classification of wind turbines based on rotor diameter is proposed in Table 1 in order to bring consistency to the discussion. Conventional large-scale horizontal axis wind turbines are well documented and spread over many territories. The main approach adopted by wind turbine manufacturers to design and analyze rotor blades is based on the blade-element/ momentum theory introduced by Glauert [3]. It

combines the one-dimensional axial momentum theory introduced by Rankine and Froude and airfoil data to compute local force on a blade element. Assumptions and theoretical developments are for example presented by Sørensen in Ref. [4] and some key results are recalled below. In the one-dimensional axial momentum theory the rotor has an infinite number of blades and the velocity of the fluid in the wake is purely axial which implies no rotation of the wake. For an incoming flow of air of density  $\rho$  with a freestream velocity  $V_\infty$ , the available power is  $P_a = \frac{1}{2}\rho\pi R_T^2 V_\infty^3$  where  $R_T$  is the radius of the rotor. The mechanical power produced by the wind turbine is  $P = \tau\omega$  with  $\tau$  the mechanical torque and  $\omega$  the angular velocity. The power coefficient  $C_p$  and the tip-speed ratio  $\lambda$  are defined as:

$$C_p = \frac{P}{P_a} = \frac{P}{\frac{1}{2}\rho\pi R_T^2 V_\infty^3} \quad (1)$$

\* Corresponding author.

E-mail address: martin.bourhis@ensam.eu (M. Bourhis).

## Nomenclature

$\rho$	Density of the fluid
$\mu$	Dynamic viscosity
$V_\infty$	Free stream wind velocity
$N$	Number of blades
$Re$	Reynolds Number
$dm$	Elementary mass of fluid
$d\dot{m}$	Elementary mass flow-rate
$R_H$	Hub radius
$R_T$	Tip radius
$H$	Hub ratio
$a$	Axial induction factor
$c$	Chord
$\sigma$	Blade solidity
$\lambda$	Tip-speed ratio
$\lambda_r$	Local tip-speed ratio
$\omega$	Angular velocity
$r$	Radial coordinate
$z$	Axial coordinate
$\alpha$	Angle of attack
$\varphi$	Rel. wind angle
$\beta$	Blade angle
$p_0$	Atmospheric pressure
$\Delta p$	Differential pressure
$T$	Temperature
$C$	Absolute velocity
$U$	Rotating velocity
$W$	Relative velocity
$C_p$	Power coefficient
$C_{p,max}$	Maximum power coefficient
$C_\tau$	Torque coefficient
$P_a$	Available power
$P$	Mechanical power
$\tau$	Torque
$C_D$	Drag coefficient
$C_L$	Lift coefficient
$C_F$	Resulting force coefficient
$C_n$	Normal load coefficient
$C_t$	Tangential load coefficient
$U$	Voltage
$I$	Current intensity
$R$	Electrical resistance
1	Upstream of the rotor
2	Downstream of the rotor

**Table 1**  
Classification of horizontal axis wind turbines based on rotor diameter. Power coefficient ( $C_p$ ) and tip-speed ratio ( $\lambda$ ) are the typical ranges in the literature.

	Rotor diameter (m)	$\lambda$	$C_p$
Micro-scale	<0.20	0–2	0.05–0.15
Centimeter-scale	0.20–0.50	2–5	0.20–0.35
Small-scale	0.50–5.0	4–8	0.35–0.50
Large-scale	>5.0	6–9	0.40–0.50

$$\lambda = \frac{R_T \omega}{V_\infty} \quad (2)$$

According to the one-dimensional axial momentum theory depicted in § 3.1 of Ref. [4], the rotor acts as a singularity which produces

a pressure drop and a velocity defect in the wake. In the model, a constant discharge velocity in the rotor plane  $C$  is defined as:

$$C = (1 - a)V_\infty \quad (3)$$

where  $a$  is the axial induction factor. Then the power coefficient associated to the power that can be extracted from an inviscid flow reads:

$$C_p = 4a(1 - a)^2 \quad (4)$$

By differentiating  $C_p$  with respect to  $a$ , the maximum power coefficient  $C_{p,max} = 16/27 \approx 0.59$  is obtained for  $a = 1/3$ . This result is commonly referred to as the Betz limit and states that no more than 59% of the available power could be transformed into mechanical power [5].

However, the previous approach does not take into account the rotation of the wake induced by the rotation of the blades. Negligible at high tip-speed ratio, it can dramatically affect wind turbine's performance at low tip-speed ratio. Glauert [3], Sørensen [4], Burton [6], Joukowski [7] and Wood [8] have proposed modified versions of the one-dimensional axial momentum theory to design an optimum rotor while taking into account the expansion and rotation of the wake by applying the angular momentum balance on a radially discretized stream tube. The maximum power coefficients for the proposed rotor models are quite similar and close to the Betz's limit at high tip-speed ratio  $\lambda$  but differ at low tip-speed ratio where it decreases towards zero, contrary to the Betz's model which assumes a constant maximum power coefficient for the whole range of tip-speed ratio. For instance, at  $\lambda = 1$ , the Glauert's model predict a maximum power coefficient  $C_{p,max} = 0.416$  and a modified Joukowski model  $C_{p,max} = 0.500$  (§ 5.2 in [4]). Moreover, these models can be improved by adding tip-losses factor to correct the assumptions of a rotor with an infinite number of blades. Then, the final design is usually made with the blade-element theory that consists of using isolated airfoils data in order to define the chord and pitch angle distributions. The following discussion is based on literature review and supported by Tables 1 and 2.

Large-scale horizontal axis wind turbines usually operate at high tip-speed ratio ( $6 \leq \lambda \leq 9$ ) and achieve power coefficient of the order of  $C_p \approx 0.5$ . At large-scale and high tip-speed ratio, the non-modified one-dimensional axial momentum theory combined with the blade-element theory is adapted to design efficient wind turbines. The rotation of the wake induced by the rotation of the blades and the tip-losses have hardly no impact on their performances because of their high operating tip-speed ratio and high dimension.

Small-scale wind turbines, with a rotor diameter ranging from 0.5 m to 5 m achieve equal power coefficient in a quasi-equivalent range of tip-speed ratios (see Table 1) and are often designed using the same method as large-scale wind turbines (please see first part of Table 2). The prediction of the performance at this scale with the blade-element/momentum theory remains quite efficient. Some authors modified the classical blade-element/momentum theory by applying correction factors that result in a change of the chord and blade angle distributions in order to match experimental and theoretical results. At small scale, some of them found a good agreement between experimental results and those predicted by the blade-element/momentum theory [9,12] and others suggested that the available experimental data were insufficient to evaluate the reliability of the theory [10] or obtained lower  $C_p$  than the expected value [16].

Centimeter-scale wind turbines and micro-scale wind turbines are designed to operate at low wind speed and for low power applications. By reducing the size of the rotor and the rated wind speed, the Reynolds number decreases and the reliability of the classical blade-element/momentum theory to design an efficient rotor becomes a controversial issue. Centimeter-scale wind turbines with a rotor diameter between 200 mm and 500 mm, designed according to the blade-element/momentum theory achieve relatively low power coefficient —typically in the range  $0.20 \leq C_p \leq 0.35$  while operating at low tip-speed ratio  $2 \leq \lambda \leq 5$  as shown in Table 1, and second part of Table 2.

**Table 2**

Summary of the literature review on small-scale and centimeter-scale wind turbines. BEM is the abbreviation for blade-element/ momentum theory.  $\lambda_{design}$  is the designed tip-speed ratio and  $\lambda_{max}$  the tip-speed ratio related to  $C_{p,max}$ .

Authors	Rotor diameter (mm)	Design method	$N$	$\lambda_{design}$	$C_{p,max}$	$\lambda_{max}$
Elizondo et al. [9]	2900	BEM	3	–	0.40–0.45	6–7
Refan et al. [10]	2200	–	3	–	0.49	9
Singh et al. [11]	1260	BEM	2	6.6	0.29	6–7
Monteiro et al. [12]	1200	–	3	5	0.40	4.8
Lee et al. [13]	1000	BEM	3	5	0.469	5.61
Akour et al. [14]	1000	BEM	3	5	0.38	4.4
Abdelsalam et al. [15]	1000	BEM	3	4	0.426	5.1
Rotor diameter (mm)						
Nishi et al. [16]	500	BEM, tip chord = 0	3	5	0.240	5
	500	BEM, tip chord = 33.3 mm	3	5	0.335	4.5
Hirahara et al. [17]	500	fan type, lin. chord, lin. twisted	4	3.3	0.4	2.7
Kishore et al. [18]	400	const. chord, non-lin. twisted	3	–	0.32	4.1
Kishore et al. [2]	394	lin. twist & tapering	3	–	0.14	2.9
Mendonca et al. [19]	200	BEM	3	3	0.29	3
Rotor diameter (mm)					Efficiency <sup>a</sup>	
Chu et al. [20]	120	Biomimetic design	3	–	0.087	3.2
Mendonca et al. [19]	100	BEM	4	1	–	1.2
Xu et al. [21]	76	Fan type	4	–	0.075	1.4
Rancourt et al. [22]	42	Fan type	4	–	0.095	0.8
Perez et al. [23]	40	–	4	–	0.058	0.75
Zakaria et al. [24]	26	Fan type	8	–	0.034	
Howey et al. [25]	20	Shrouded ducted type	12	1	0.09	0.6

<sup>a</sup>The efficiency given here is the ratio of the electrical power to the available wind power and is thus the product of  $C_p$  with unknown mechanical and electrical efficiencies.

Finally, micro-scale wind turbines, with a diameter of the rotor lower than 200 mm, exhibit lower  $C_p$  in the range  $0.05 \leq C_p \leq 0.15$  and operate at very low tip-speed ratio  $0 \leq \lambda \leq 2$  [19–24]. At micro-scale, no author applied the classical blade-element/ momentum theory to design an optimum rotor and analyze their wind turbines. The direct implementation of the blade-element/ momentum theory for the design of micro-scale and centimeter-scale wind turbines does not appear reliable for several reasons described below.

Firstly, they face the issue of operating at low Reynolds number. Indeed, because of their small size and low operating wind speed, their profiles may undergo laminar separation bubble, a phenomena that appears at the transition from the laminar to turbulent flow [26,27]. The aerodynamic properties of blade profiles differ from the ones obtained at high Reynolds number. The laminar flow detaches from the surface of the blade due to too high adverse pressure gradient that causes an increase of the size of the boundary layer and a loss of aerodynamic lift. Large-scale wind turbines are not confronted to these issues because they operate at high Reynolds number where the boundary layer's detachment is postponed to higher adverse pressure gradients. The choice of a particular airfoil also plays a major role in the aerodynamic performance of a wind turbine to avoid laminar separation bubble. A specific geometry can help to reduce the suction peak at the leading edge of the blade in order to prevent a too high adverse pressure gradient on the upper surface that can lead to separation of the flow at the surface. Thin profiles such as *SG60xx* series studied by Giguere and Selig [26,28] show good performance at low Reynolds number. Some authors have reported performance improvement by increasing the leading edge nose radius, or by cusping the trailing edge [11]. A study performed by Lissaman et al. [29] stated that a small degree of roughness was associated with higher performance at low Reynolds number conditions.

Secondly, at small scale, wind turbines must generate enough torque to overtake friction losses between all mechanical parts even at low wind speed. As the mechanical power is equal to the product of torque times the angular velocity of the wind turbine, at a given power level, the higher the torque, the lower the angular velocity should be. Thus, at small scale, wind turbines should have low rotating speed and therefore a low tip-speed ratio. From the study of wind turbines in the same diameter range as in the present study, many authors concluded that a

very low optimal tip speed ratio in the range of  $1 \leq \lambda \leq 3$  is suitable for small size rotors [17,19,21]. Indeed, for a given wind speed, the torque must be as high as possible in order to overtake the resistive torque of the mechanical parts contained in the nacelle and to start rotation and power production. The review on micro-scale wind turbines has shown that they operate at a very low tip-speed ratio  $0 \leq \lambda \leq 2$  (see bottom part of Table 2). In return, a high torque induces a high rotation of the fluid in the wake and significant losses. As mentioned before, various models based on the angular momentum balance have been proposed to take into account the rotation of the wake [3,4,6–8]. For tip-speed ratios in the range  $3 \leq \lambda \leq 6$ , the differences in pitch and chord distributions between the various models appear to be significant only in the inner 25%–50% of the rotor. But for tip-speed ratio of the order of  $\lambda = 1$ , the different models lead to significantly different designs of the blades from the root to the tip, with a dramatic increase of the chord distribution at the root for some of these models. Thus, as noticed by Sharpe [30], the solidity of the blade cascade could become as high as the assumption that the airfoils are isolated may no longer hold. Consequently, the reliability of the classical blade-element/ momentum theory for the design of an optimum rotor is still a controversial issue for wind-turbines operating at very low tip-speed ratio [4,30].

Studies on micro-scale wind turbines have shown other interesting results for the design of the 300 mm wind turbine presented in this paper. Leung et al. [31] compared various configuration of micro fan bladed wind turbine and concluded that multiblade and high solidity rotors (greater than 50%) are suitable for micro scale wind turbines. Duquette et al. [32] also concluded that an increase of blade solidity and number of blades are associated with an increase of  $C_p$ . A 100 mm multi-bladed wind turbine designed according to the Joukowski optimum rotor model with a  $\lambda_{design} = 1$  is mentioned in § 6.5 of Ref. [4]. To summarize the literature review on micro-scale wind turbines, most of them have multiple fan-type blades, operate at low tip-speed ratio and have lower  $C_p$  than large-scale wind turbines [20–22,24,31].

Few authors worked on centimeter-scale wind turbines with a diameter between 200 mm and 500 mm. At this scale some authors tried to apply the blade-element/ momentum theory with various corrections and others presented chord and blade angle distribution based on the experience. Some results are presented in the central part of Table 2. Kishore et al. [18] designed a 3-bladed wind turbine with a diameter of

400 mm with a constant chord and non linearly twisted. They obtained a peak efficiency of 21%. Hirahara et al. [17] designed a 500 mm rotor linearly twisted and obtained a maximum power coefficient  $C_{p,max} = 0.4$  for  $\lambda = 2.7$ . Nishi et al. [16] manufactured two 50 mm rotors according to the classical blade-element/ momentum theory with Prandtl's tip loss factor but with different tip chord length. They obtained a 38.7% higher  $C_{p,max}$  with the increase of the tip chord length. However, these studies present wind turbine with high design and optimum tip-speed ratio where the classical blade-element/ momentum theory gives quite efficient results. To the best of our knowledge, very few experiments with a centimeter-scale wind turbine operating at very low tip-speed ratio are available in the literature.

Thus, the aim of this study is to investigate experimentally the performances and the wake of a 300 mm horizontal-axis wind turbine operating at low tip-speed ratio ( $\lambda = 1$ ). This turbine is designed with a new method based on blade cascade arrangement and detailed in Section 2. Few papers in the open literature present experimental data of a wind turbine with a same size of rotor and/or operating at low tip-speed ratio. We compare the experimental results of the innovative wind turbine, to a more classical 300 mm and 3 bladed horizontal-axis wind turbine with a higher tip speed ratio ( $\lambda = 3$ ) selected in accordance with the review presented in Table 2. A detailed investigation of the aerodynamic performance (torque and mechanical power as a function of the angular velocity for the entire operating range) was performed in a wind tunnel. Moreover, a broad wake analysis by stereoscopic particle image velocimetry processing were carried out. The experimental apparatus are presented in Section 3. Finally, the results are presented in Section 4 and discussed in Section 5.

## 2. Design methods

Key points and equations for the design of the reference wind turbine are depicted in § 2.1, then the new design method based on the design of a suitable blade cascade is detailed in § 2.2. Both wind turbines are designed with the following design brief. The working fluid is air with  $\rho = 1.2 \text{ kg.m}^{-3}$  and  $\mu = 1.8 \times 10^{-5} \text{ Pa.s}$ . The design free stream wind velocity is set at  $V_\infty = 10 \text{ m.s}^{-1}$ . The selected rotor radius and hub radius are respectively set at  $R_T = 150 \text{ mm}$  and  $R_H = 45 \text{ mm}$ . The hub ratio  $H = \frac{R_H}{R_T}$  is thus equal to 0.3 for both wind turbines. This value, relatively high compared to large-scale wind turbines, is linked to the geometric constraint imposed by the equipment placed in the nacelle. In both design methods, the equations from the classical one-dimensional axial momentum theory are used (see Eq. (3) &(4)): the design axial induction factor is set at  $a = 1/3$  and the corresponding inviscid  $C_p$  is used to compute the mechanical power.

The chord and pitch angle distributions are computed in two distinct ways: with the blade element method that considers the lift of isolated airfoils, and by designing high solidity blade cascades with a prescribed wake vortex law. For easier reading, the wind turbine designed according to the blade-element/ momentum theory is named BWT and the other, designed by coupling the angular momentum balance to blade cascades, is the EWT. The design parameters of the two wind turbines are summarized in Table 3, and the resulting chord length, pitch angle and blade cascade solidity as a function of the radius are presented in Fig. 3.

### 2.1. BWT design method

A more classical three-bladed wind turbine is first designed with a tip-speed ratio  $\lambda = 3$ . Its design tip-speed ratio has been chosen to be within the typical tip-speed ratio range of wind turbines with similar dimensions (see Table 2). The radial distributions of chord and pitch angle are computed with the one-dimensional axial momentum theory coupled to the blade element method that uses the local aerodynamic force on the blades with the help of airfoil data. The SG6042 airfoil has been selected because of the high lift-to-drag performances at low

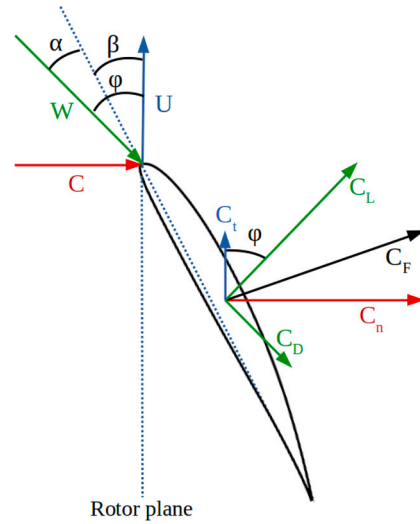


Fig. 1. Velocity triangle and projections of the aerodynamic coefficients on the SG6042 airfoil.

Reynolds number [26,28]. This airfoil is widely used for small-scale wind turbines. The polar plot of the SG6042 airfoil at  $Re = 10^5$  has been digitized from Ref. [33] in order to obtain the lift and drag coefficients. The maximum lift-to-drag ratio  $C_L/C_D \approx 53$  is obtained for the optimum angle of attack  $\alpha_0 = 6^\circ$ . It corresponds to  $C_L \approx 0.99$  and  $C_D \approx 0.019$ . A constant angle of attack  $\alpha_0$  along the span is assumed in the design settings. Then, the local blade pitch angle  $\beta(r)$ , that is the angle between the chord line and the rotation plane, is calculated using the velocity triangle (see Fig. 1) and the Eq. (5) for 11 blade sections:

$$\beta(r) = \arctan\left(\frac{C}{U(r)}\right) - \alpha_0 \quad (5)$$

In Eq. (5),  $C$  is the axial velocity in the rotor plane and  $U$  is the rotational speed of the rotor. The chord  $c$  is computed for the 11 blade sections using Eqs. (6) to (8), in which  $\varphi$  is the angle between the relative velocity and the rotation plane and  $\sigma$  is the local blade cascade solidity, defined as the ratio of the blade chord length to the azimuthal pitch distance.

$$C_n = C_L \cos(\varphi) + C_D \sin(\varphi) \quad (6)$$

$$\sigma(r) = \frac{4a \sin^2(\varphi)}{(1-a)C_n} \quad (7)$$

$$c(r) = \frac{2\pi r \sigma(r)}{N} \quad (8)$$

The chord length varies from  $c = 82 \text{ mm}$  at the root to  $c = 30 \text{ mm}$  at the tip with an average chord length of 45 mm. The blade is non-linearly twisted and the pitch angle decreases from  $\beta = 31^\circ$  to  $\beta = 6.5^\circ$  (see Fig. 3).

Some corrections could have been taken into account for blade's design such as the Glauert correction to include the rotation of the wake. However, as mentioned in the introduction, few differences in the design are noticed when  $H(r) = r/R_T$  is high. Moreover, various engineering corrections such as tip corrections could be implemented in the design method of this wind turbine but it is not the concern of this paper.

### 2.2. EWT design method

Micro-scale and centimeter-scale wind turbines need a high starting torque to produce power at low wind speed by overtaking friction torque of the different mechanical parts. To achieve this purpose, a low tip-speed ratio and multi-bladed wind turbine is suitable [17,19,21].

**Table 3**

Wind turbines design parameters. The range of Reynolds number from the root to the tip of the blades is computed according to  $Re = \rho Wc/\mu$  where  $W$  is the relative velocity.

	$R_T$ (mm)	$P(W)$	$H$	$a$	$\lambda$	$N$	Airfoil	$\alpha(^{\circ})$	$\sigma(R_H)$	$\sigma(R_T)$	$Re$
BWT	150	25.13	0.3	1/3	3	3	SG6042	6	0.87	0.10	61400–61900
EWT	150	25.13	0.3	1/3	1	8	NACAx10	x	1.65	0.70	28500–66200

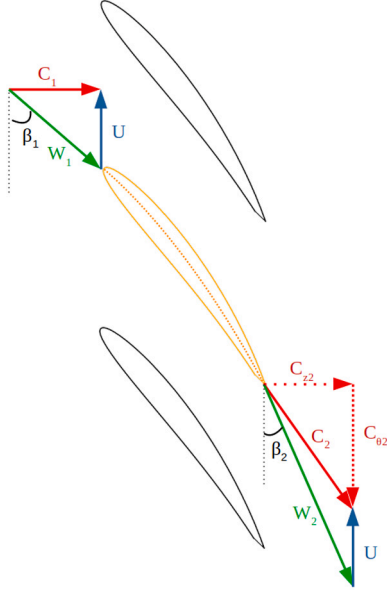


**Fig. 2.** Blade cascade and velocity triangle for the EWT. Index 1 refers to upstream of the rotor and 2 downstream of it.  $U$  is the rotating velocity of the rotor,  $W$  the relative velocity in the turbine's reference frame and  $C$  the absolute velocity.

A decrease of the tip-speed ratio results in a significant rotation of the fluid in the wake. According to the angular momentum balance, the torque applied by the rotor on the fluid is linked to the amount of tangential velocity. Thus, the main purpose of the proposed design method is to force the fluid to follow a geometric deflection by constraining it into a blade cascade arrangement. The first step of the design method is to compute an expectative tangential outlet velocity distribution with the Euler's turbomachinery theorem and then to design a blade cascade geometry able to impose the required geometric deflection to the fluid.

On this basis, the Euler's turbomachinery equation *i.e* the angular momentum balance is applied on an annular disc between  $r$  and  $r + dr$  and reads:

$$d\tau = d\dot{m}(C_{\theta 2}r - C_{\theta 1}r) \quad (9)$$

where  $d\tau$  is the elementary torque applied by the rotor on the fluid,  $C_{\theta}$  the tangential velocity of the fluid and  $d\dot{m}$  the elementary mass flow-rate. The index 1 refers to upstream of the rotor and 2 to downstream of it. An axial upstream wind speed  $C_1 = V_{\infty}(1 - a)$  is assumed and therefore the upstream tangential velocity is assumed to be  $C_{\theta 1} = 0$ . The elementary mass of fluid that goes through the annular disc between times  $t$  and  $t + dt$  is  $dm = \rho 2\pi r dr C_1 dt$ . The associated elementary mass flow-rate is  $d\dot{m} = \rho 2\pi r dr C_1$ . The elementary power transferred from the fluid to the rotor is obtained by multiplying the previous equation by the angular rotating speed of the rotor:

$$dP = d\dot{m}C_{\theta 2}U_2 \quad (10)$$

By integrating on the whole span:

$$P = \int_{R_H}^{R_T} d\dot{m}C_{\theta 2}U_2 \quad (11)$$

$$P = 2\pi\rho V_{\infty}\omega \int_{R_H}^{R_T} (1 - a)r^2 C_{\theta 2} dr \quad (12)$$

At this step, various axial induction factor radial profiles  $a(r)$  and various vortex distributions  $C_{\theta 2} = f(r)$  can be considered. For instance, the basic assumption of the Joukowski model is that the rotor is subject to a constant circulation, hence the tangential velocity is given as  $C_{\theta 2} = cte/r$  (free vortex law) [7]. Once a choice has been made for the vortex distribution, the previous equations of the blade element theory (Eq. (6), (7), (8)) may be used to compute chord and blade angle distributions by adding a tangential induction factor  $a' = -C_{\theta 2}/2r\omega$ . However, a decrease of  $\lambda$  induces an increase of the relative wind angle  $\varphi$  and then an increase of the blade pitch angle and solidity (Eq. (7)). The lift and drag coefficients that are used in Eq. (8) are obtained from isolated and two-dimensional airfoils data. The increase of the blade solidity can lead to an unknown mutual blade interactions and consequently the accuracy of airfoils data is questionable.

To cope with uncertainties on aerodynamic coefficients, the new design method freed from airfoils data. The main purpose is to impose a geometric deflection to the fluid *i.e* a specific vortex law  $C_{\theta 2} = f(r)$ , by constraining it into a blade cascade arrangement. Forced vortex, free vortex or other distributions can be considered but for the design of the actual wind turbine one arbitrarily assumes a uniform axial velocity and a constant vortex law  $C_{\theta 2} = cst$ , that corresponds to a linear increase of the blade work along the span as a first try. Thus, the Eq. (12) reads:

$$P = 2\pi\rho(1 - a)V_{\infty}\omega C_{\theta 2} \int_{R_H}^{R_T} r^2 dr \quad (13)$$

$$P = 2\pi\rho(1 - a)V_{\infty}\omega C_{\theta 2} \left[ \frac{R_T^3}{3} - \frac{R_H^3}{3} \right] \quad (14)$$

With these assumptions and using the same target power as in the BWT design, the tangential velocity of the fluid downstream of the rotor is given by:

$$C_{\theta 2} = \frac{C_p P_a}{2\pi\rho(1 - a)V_{\infty}\omega \left[ \frac{R_T^3}{3} - \frac{R_H^3}{3} \right]} \simeq 6.8 \text{ m s}^{-1} \quad (15)$$

The velocity triangle allows the computation of the blade angles at the input and output of the rotor (Fig. 2).

$$\beta_1 = \arctan\left(\frac{V(1 - a)}{r\omega}\right) \quad (16)$$

$$\beta_2 = \arctan\left(\frac{V(1 - a)}{C_{\theta 2} + r\omega}\right) \quad (17)$$

Then, at each radius, a polynomial camber mean-line tangent to the relative velocity at the leading and trailing edges is drawn according to:

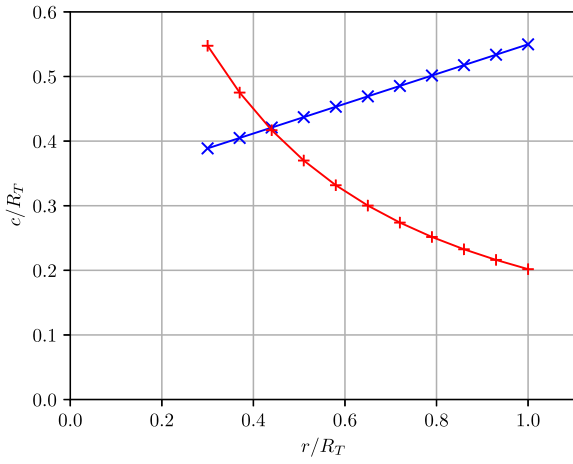
$$y = \frac{\tan(\beta_2) - \tan(\beta_1)}{2} x^2 + \tan(\beta_1)x \quad x \in [0; 1] \quad (18)$$

such that the previous blade conditions are satisfied:

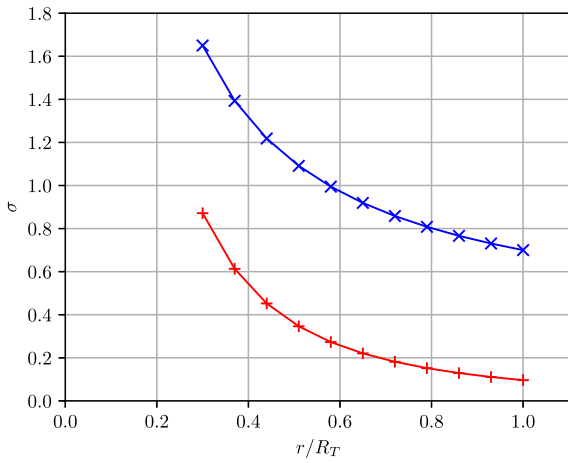
$$\left(\frac{dy}{dx}\right)_0 = \tan(\beta_1) \quad (19)$$

$$\left(\frac{dy}{dx}\right)_1 = \tan(\beta_2) \quad (20)$$

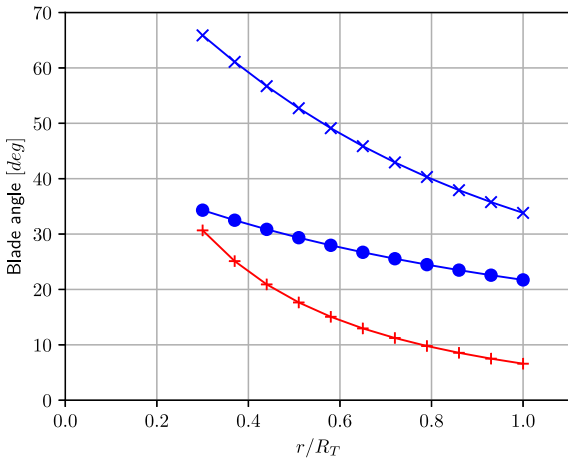
Moreover, to ensure the required flow deviation, a high solidity and a significant number of blades are arbitrarily imposed. The chord length is computed on these basis. According to the literature on usual axial gasturbines, the solidity should be of the order of  $\sigma \simeq 1$  to ensure the required flow deviation with acceptable losses [34].



(a)



(b)



(c)

Fig. 3. Geometry distributions as a function of normalized radial coordinate for the EWT (×) and for the BWT (+). (3(a)): chord length; (3(b)): blade solidity  $\sigma = \frac{Nc}{2\pi r}$  and (3(c)): pitch angle  $\beta$  for the BWT (Fig. 1) and blade angles at the input  $\beta_1$  (×) and output  $\beta_2$  (●) of the EWT (Fig. 2)

The final design of the EWT has been done with the parameters mentioned in the first paragraph of this section for a tip-speed ratio

$\lambda = 1$ . The number of blades is  $N = 8$ . The chord distribution is linear and is computed according to Eq. (8), with respectively a blade cascade solidity at root  $\sigma(R_H) = 1.65$  and at tip  $\sigma(R_T) = 0.7$ . Thus the resulting chord length varies linearly from 58 mm at the root to 82 mm at the tip with a mean chord length of 70 mm (see Fig. 3). Finally, the thickness distribution is calculated according to the equation of the symmetrical NACAxx10 airfoil.

As shown in Table 3, both wind turbine operate at low Reynolds number  $Re$  compared to large scale wind turbines, in the range of  $28500 \leq Re \leq 66200$  from the root to the tip of the blades for EWT, the BWT presenting fewer variation of  $Re$  along the span ( $61400 \leq Re \leq 61900$ ). In this range of  $Re$ , the flow regime is closed to the laminar-turbulent transition at which viscous effects can alter aerodynamic properties of airfoils and wind turbine performance. CAD pictures of the two wind turbines are moreover available in Fig. 4.

### 3. Experimental setup

In order to investigate experimentally the wind turbines performance, both prototypes were manufactured by stereolithography to obtain an equal degree of roughness.

#### 3.1. Performance

The performance of both wind-turbines were evaluated in terms of power coefficient  $C_p$  and torque coefficient  $C_\tau = \frac{C_p}{\lambda}$  for various tip-speed ratios. The experimental study is carried out in the Prandtl type wind tunnel of the LIFSE facilities (Fig. 5). The closed loop wind tunnel has a semi-open test section and an axial fan with a rotor diameter of 3 m controlled by an asynchronous motor. Behind the fan, the flow is decelerated and straightened in a settling chamber equipped with honeycomb strengtheners. Upstream of the test section, the flow is accelerated by means of a tunnel nozzle with a contraction ratio of 12.5. The test section has a cross-section  $1.35 \times 1.65 \text{ m}^2$  and is 1.80 m long. It is followed by a slowly diverging section with  $3^\circ$  half angle and 10 m in length.

The turbine is mounted on an 530 mm tall mast with a 700 mm long nacelle containing a rotating shaft on which a rotating torque meter HBM-TW20 and a MAXON DC motor are anchored (Fig. 5). The contactless torque transducer with range 2 N.m and accuracy of 0.002 N.m ensures the coupling between the rotor shaft and the generator. Moreover, it delivers 360 pulses per revolution and thus allows angular velocity measurement. The generator is wired to resistors and is used as a brake system by imposing a resistive torque to the wind turbine. Characteristics of the generator  $U = f(\omega)$  and  $I = f(\tau)$  have previously been determined. The voltage at the generator terminals is proportional to the angular velocity of the shaft for  $0V \leq U \leq 35V$  according to  $U = 0.124\omega$  with a coefficient of determination  $R^2 = 0.9975$ . The electrical current through the resistance varies linearly with the torque according to  $I = 8.27\tau - 0.23$  with a coefficient of determination  $R^2 = 0.9955$ . The residual torque at zero current is a measure of the static friction torque of the bearings placed between the torque transducer and the generator. The static torque is systematically measured and removed from acquisitions but frictional losses in the bearing have not been included in the computation of the power coefficient. The atmospheric pressure  $p_0$  and temperature  $T$  are consistently recorded during the acquisitions in order to evaluate air density  $\rho = \frac{p_0}{rT}$  with  $r$  the specific gas constant for air. The wind speed is calculated with the measurement of the dynamic pressure  $P_d$  via a Pitot probe placed in the wind tunnel  $V_\infty = \sqrt{\frac{2P_d}{\rho}}$ .

The wind speed in the tunnel is kept approximately constant at  $V_\infty = 10 \text{ m.s}^{-1}$  whereas the resistive torque on the wind turbine is modified between each acquisition by changing the voltage to the generator. All acquisitions are made at constant resistive load on the generator. The signals of  $T$ ,  $P_d$ ,  $\tau$  and  $\omega$  are recorded at a sampling frequency of 1000 Hz and digitized using an NI USB6229 acquisition card. For

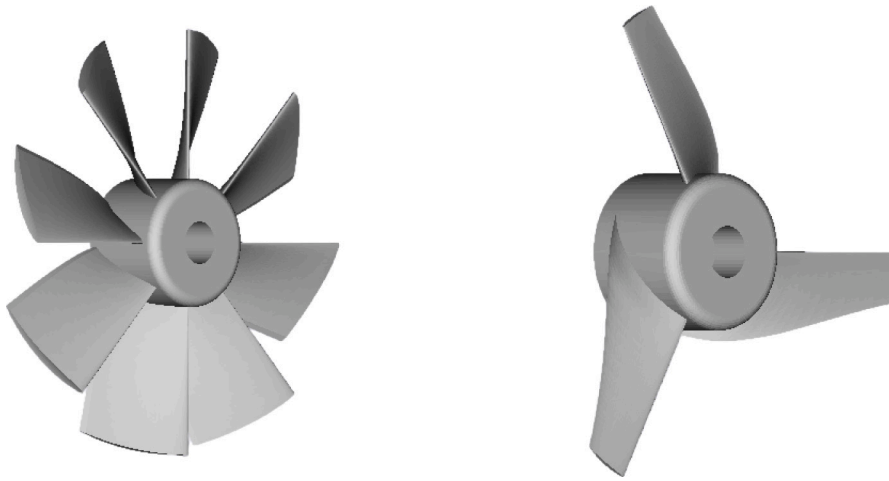


Fig. 4. CAD of the EWT and BWT.

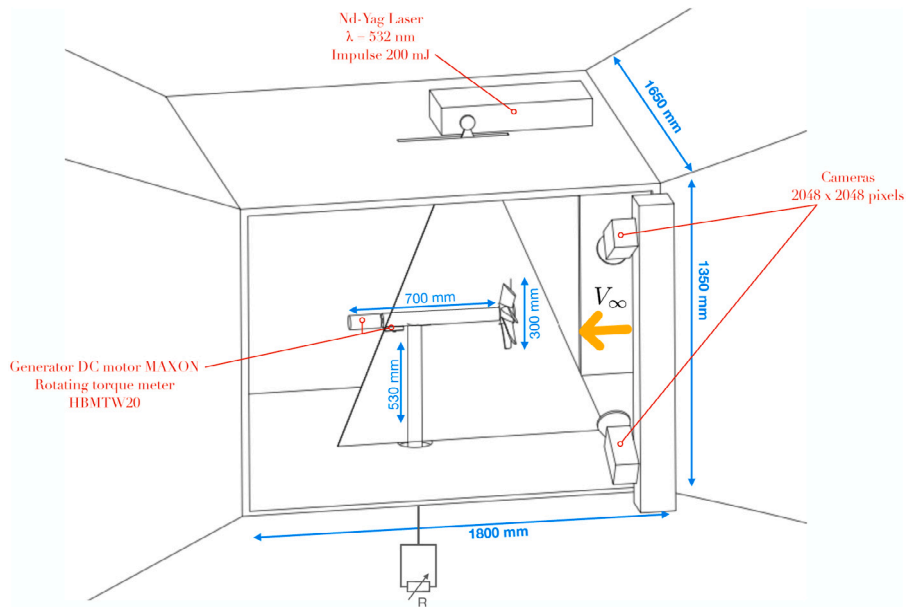


Fig. 5. Detailed schematic of the open-jet wind tunnel of the LIFSE facilities (the diverging part is not to scale). The equipment for the stereo-PIV and  $C_p = f(\lambda)$  curve are represented on the figure.

various resistive load, 50 samples of 0.5 s are acquired and for every samples, the means of  $T$ ,  $\Delta p$ ,  $\tau$  and  $\omega$  are logged in a file text. Moreover, for each wind turbine, the experiment have been performed on several different days with various number of samples, acquisition times and sampling frequency. This results in highly reproducible  $C_p$  and  $C_t$  curves. Finally, the experimental results presented below are obtained from several test campaigns. Error bars plotted on experimental results figures represent two standard deviations for each acquisition.

### 3.2. Wake analysis by stereoscopic particle image velocimetry

The stereoscopic particle image velocimetry (stereo-PIV) is handled by DynamicsStudio, a software edited by Dantec. The stereo-PIV system is equipped with a Nd-Yag laser of wavelength 532 nm (Litron Nano-L 200-15) with an impulse power of 200 mJ. The cameras for pictures acquisitions have a resolution of  $2048 \times 2048$  pixels and are supplied with a lens (Micro-Nikkor AF 60 mm f/2.8D), a frame grabber card and a synchronization system. A Scheimpflug system is coupled to the cameras in order to make colinear the plane of interest behind the rotor,

the lens plane and the image plane. A schematic of the experimental setup is shown in Fig. 5.

The flow is continuously seeded with 2 to 5  $\mu$  m diameter drops of oil swarmed by a fog machine. The particle tracers are illuminated twice by a light sheet within the flow generated by the laser. The laser sheet is perpendicular to the plane of rotation and contains the axis of the rotor. The delay between two pulses has been set at 100  $\mu$  s in order to get a tracer's displacement of approximately a quarter of the length of the interrogation window.

Approximately 200 double frame images have been acquired with each wind-turbine mounted and operating at their optimum tip-speed ratio. After image dewarping and applying of the calibration, the local displacement vector for the images of the tracer particles of the first and second illumination is computed for each interrogation window by adaptive correlation. Then the three components of the local flow velocity into the plane of the light sheet are reconstructed by stereo-particle image velocimetry processing. Theoretical and practical developments of the particle image velocimetry are presented by Raffel et al. [35]. The origin of the physical frame is located at the intersection of the rotor axis and the plane of blade's leading edge. Two sets of acquisitions

have been conducted with different acquisition mode. Laser firing and image acquisition have first been synchronized with the blade angular position. One image is acquired at every passage of a same blade at a vertical position. Results from these acquisitions are named synchronized acquisitions. A second set of acquisitions has been performed during which laser firing and pictures acquisitions are triggered by an internal clock set at 2 Hz. This triggering mode allows the acquisition of images for various angular position of the rotor. By acquiring 200 double frame images, the velocity fields are computed by doing a simple mean on the whole azimuth for each velocity components. A modification of the frequency acquisition (1 Hz) or in the number of acquired images (from 50 to 500) results in a variation of the average velocities lower than  $0.2 \text{ m.s}^{-1}$ . Moreover, beyond 200 acquired images, the variation on the velocity fields remains constant and lower than  $0.2 \text{ m.s}^{-1}$ . Results from these acquisitions are named non-synchronized acquisitions. Stereo-PIV acquisitions have been acquired for both wind turbines operating at their optimum tip-speed ratio.

## 4. Results

### 4.1. Performance analysis

In this section, comparisons between the experimental results obtained from the two rotor designs are presented and discussed. Experimental plots of  $C_\tau(\lambda)$  are presented in Fig. 6(a). The starting torque coefficient *i.e.*  $C_\tau(\lambda = 0)$  of the EWT is equal to 0.523. For comparison the starting torque coefficient of the BWT is equal to  $C_\tau = 0.03$ . As the ratio of the EWT starting torque to the BWT starting torque is approximately equal to 16, the EWT will generate the same torque at  $\omega = 0 \text{ rad.s}^{-1}$  with 4 times lower wind speed than the BWT. The cut-in wind speed of both wind turbines have been measured in order to compare their behavior at very low wind speed. For this purpose, the resistor is disconnected from the generator and the wind speed is gradually increased. The instantaneous cut-in wind speed is defined as the speed at which the wind turbine begins to rotate without stopping and without manual intervention. Thus, the wind turbine must overtake the friction torque of the mechanical parts contained in the nacelle. The measured value of the cut-in wind speed is  $2.4 \text{ m.s}^{-1}$  for the EWT and  $7.9 \text{ m.s}^{-1}$  for the BWT. The ratio of the cut-in wind speed is of the same order of magnitude as the starting torque ratio.

The EWT's torque coefficient decreases linearly with the tip-speed ratio according to  $C_\tau = -0.226\lambda + 0.523$  with a coefficient of determination  $R^2 = 0.9979$ . The EWT is able to operate in a wide range of torque, from  $C_\tau = 0.523$  at  $\lambda \approx 0$ , to  $C_\tau = 0.05$  at  $\lambda = 2$ . For comparison, the maximum torque coefficient of the BWT is  $C_\tau = 0.126$  and occurs at the tip-speed ratio  $\lambda = 2.3$ . Its range of  $C_\tau$  is limited from 0.03 at  $\lambda \approx 0$  to its maximum value. Moreover, for the BWT, one can notice that no steady experimental data points are displayed in the  $C_p(\lambda)$  and  $C_\tau(\lambda)$  curves in the range  $0.7 \leq \lambda \leq 2.3$ . This is due to the fact that the torque as a function of the angular velocity does not behave monotonically: the torque coefficient of the BWT first increases with  $\lambda$  from  $\lambda = 0$  to  $\lambda \approx 2.3$  and then decreases. Thus, there is a range of corresponding  $\lambda$  for which the characteristic curve  $\mathcal{U} = f(I)$  of the generator with the BWT mounted on it does not present any intersection point with the characteristic curve of the load  $\mathcal{U} = \mathcal{R}I$  for the associated range of resistive load. Thus, with the present direct coupling of the DC generator to a resistive load, there is an unstable branch for the BWT: the system skips from an operating point at one end of the first branch to another operating point on the second branch in a transient way. Torque and angular velocity have been measured during two transients and the paths that have been followed in the phase space of the system are displayed with dashed lines in Fig. 6. The black triangles (►) indicate the direction of variation of the curve. The path between two stable operating points differs under the increase/decrease of the load *i.e.* the decrease/increase of the tip-speed ratio. The duration of the transient depends on the mechanical inertia of the system and is here

of the order of a few hundreds of seconds. Moreover, for a given torque coefficient  $C_\tau$ , the BWT presents several operating points corresponding to different values of  $\lambda$ . One operating point is stable and the two others, located on the transient curves, are unstable and lead to an acceleration or a deceleration of the wind turbine until a stable regime is eventually restored. Thus, with a voltage regulation by a resistor or a resisting torque control strategy, the BWT cannot operate in the whole range of tip-speed ratios.

On the contrary, the EWT has a single  $\lambda$  and thus a unique operating point for its whole range of torque coefficient. Moreover, the steep  $C_\tau(\lambda)$  curve of the EWT compared to the BWT is remarkable and could be useful for electrical applications. Indeed, the EWT can run for a wide range of load and presents a linear response of its angular velocity to a voltage regulation. These advantages could be favorable to charge a battery where a sensitive adjustment of the angular velocity is required in order to maintain it and the charging voltage constant.

We also compare the power coefficient  $C_p$  of both wind turbines for various tip-speed ratio. Experimental results of  $C_p$  are presented in Fig. 6(b). The maximum power coefficient of the EWT is  $C_{p,max} = 0.31$  and is obtained for  $\lambda = 1$ , that corresponds well to the designed tip-speed ratio. The associated mechanical power is  $P = 13.1W$ . The maximum power coefficient of the BWT is  $C_{p,max} = 0.33$  and is obtained for  $\lambda = 2.9$ . Such as reported in [16], the maximum power coefficient is lower than the predicted value by the blade-element/ momentum theory but the optimum tip-speed ratio corresponds well to the designed tip-speed ratio. The maximum mechanical power generated by the BWT is  $P = 14.0W$ . Few studies reported such good performance for this size of wind-turbine. Moreover, most of wind turbines with a diameter between 200 and 500 mm are designed for a tip-speed ratio close to 3 and have equal or fewer power coefficient [2,16–19]. To the best of our knowledge, the EWT is the first wind turbine designed to operate at  $\lambda = 1$  that achieves such performance at this scale.

### 4.2. Wake analysis

The tangential and axial velocity fields and profiles for both wind turbines are respectively presented in Figs. 7 and 8. The left column corresponds to the results obtained for the EWT and the right column to the results of the BWT. Synchronized acquisitions show, in particular, the locations of the wingtip vertices and the spiral form of the vortex in the wake.

Tangential velocity fields in Figs. 7(a), 7(c) and profiles in Fig. 7(e) for the EWT show high magnitude of tangential velocity in the wake of the EWT from  $10 \text{ m.s}^{-1}$  at a distance of  $2R_T/3$  at the level of the hub to  $6.5 \text{ m.s}^{-1}$  at a distance of  $5R_T/3$ . Moreover, the tangential velocity magnitude in the vortex center decreases with the distance from the wind turbine:  $C_{\theta 2} = 6.8 \text{ m.s}^{-1}$  at  $z = 111 \text{ mm}$  for the first center,  $C_{\theta 2} = 5.6 \text{ m.s}^{-1}$  at  $z = 190.5 \text{ mm}$  for the second center and  $C_{\theta 2} = 4.8 \text{ m.s}^{-1}$  at  $z = 267.8 \text{ mm}$  for the last one. Although the magnitude of tangential velocity is high, no recirculating bubble associated with vortex breakdown have been observed in the 500 mm downstream wake contrary to the stereo-PIV results of the multi-bladed and low tip-speed ratio wind turbine presented in § 6.5 of Ref. [4]. The wake angle, defined as the angle between the rotor axis and a straight line joining vertices centers is approximately equal to  $3^\circ$ . An equal angle is obtained from non-synchronized acquisition. The radial distance between the vortex and the rotor axis decreases by 2 mm for each center. These indicators characterize the wake expansion behind the EWT. Moreover, the axial distance between each center of vortex decreases from  $d = 79.6 \text{ mm}$  to  $d = 77.3 \text{ mm}$  which corresponds to a decrease in the length of the spiral form of vortex. Furthermore the EWT has been designed with a target tangential velocity of  $6.8 \text{ m.s}^{-1}$  in the wake in order to generate the desired power  $P$ . The assumption of a constant tangential velocity along the span made for the design of the EWT seems incorrect according to Fig. 7(e). However, the results presented in Table 4 indicate that the average tangential velocity along the span,

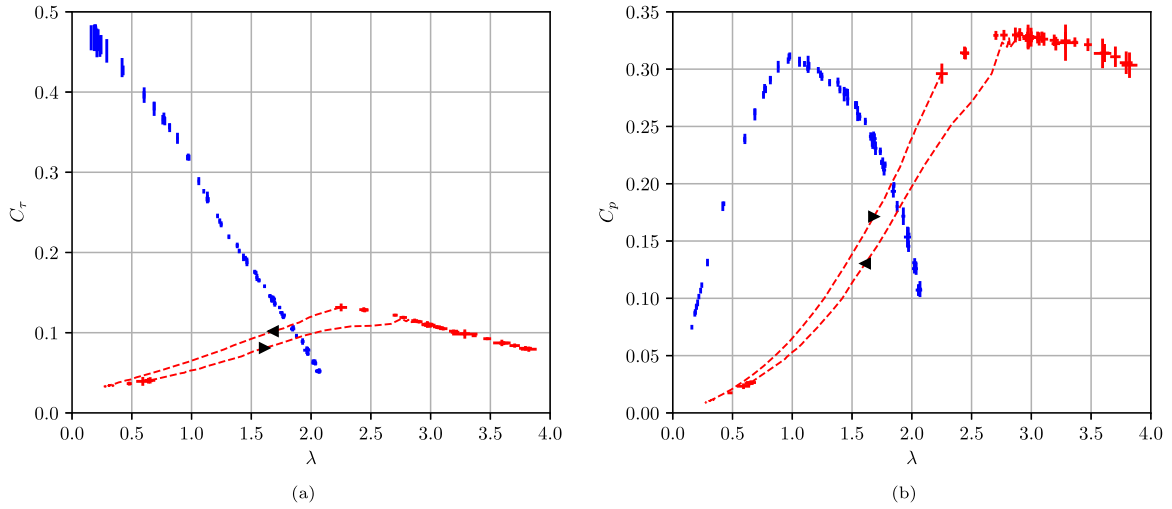


Fig. 6. Torque coefficient  $C_t$  (6(a)) and power coefficient  $C_p$  (6(b)) as a function of tip-speed ratio  $\lambda$  for the BWT (+) and for the EWT (+). Both experimental plots were obtained with a free stream wind velocity  $V_\infty = 10 \text{ m.s}^{-1}$ . The BWT present transient periods (---) that depend on the direction of variation of  $\lambda$  (►). Error bars are plotted with a 95% confidence interval.

Table 4  
Tangential velocity for the EWT.

$z$	$R_T/3$	$2R_T/3$	$R_T$	$4R_T/3$	$5R_T/3$
$z$ (mm)	52.5	100	150	200	250
$\langle C_{\theta 2} \rangle$ ( $\text{m s}^{-1}$ )	5.32	6.38	6.23	5.87	5.62
$\sigma_{C_{\theta 2}}$ ( $\text{m s}^{-1}$ )	1.54	1.56	1.28	0.9	0.21

Table 5  
Axial velocity and axial induction factor for EWT.

$z$	$R_T/3$	$2R_T/3$	$R_T$	$4R_T/3$	$5R_T/3$
$z$ (mm)	52.5	100	150	200	250
$\langle C_{z2} \rangle$ ( $\text{m s}^{-1}$ )	6.61	6.24	6.66	6.47	6.70
$\sigma_{C_{z2}}$ ( $\text{m s}^{-1}$ )	0.26	0.23	0.21	0.23	0.21
$\langle a \rangle$	0.339	0.376	0.334	0.353	0.330

i.e for  $r \in [45; 150]$  mm, are close to the design tangential velocity for various distance from the physical frame origin. The tangential velocity profiles for various distances from the EWT are very similar from root to tip. A linear interpolation from the tangential velocity profile at the distance  $z = R$  from the wind turbine has been performed. It shows that the tangential velocity decreases linearly from root to tip as follows:  $C_{\theta 2} = -0.045r + 10.402$  with a coefficient of determination  $R^2 = 0.9992$ . This discovery could be useful for the design of a new prototype with a linear expression of  $C_{\theta 2}$  rather than a constant one as assumed in the design method. The high magnitude of tangential velocity in the wake is associated with high energy losses in the rotating wake. This kinetic energy could be recovered by a contra-rotating wind turbine placed behind the EWT. Based on the design method presented in this paper, the contra-rotating wind turbine could be design with a linear expression of the tangential upstream wind speed  $C_{\theta 1,CR} = C_{\theta 2}$  and a tangential downstream velocity equal to zero  $C_{\theta 2,CR} = 0$  in order to straighten fluid streamlines and mitigate wake expansion.

The shape of axial velocity profiles of the EWT are almost similar for various distances  $z$  from the origin (see Fig. 8(e)). The axial velocity in the wake along the span of the blade is relatively constant and equal to  $C_{z2} = 6.5 \text{ m.s}^{-1}$ . As made before for the tangential velocity, the simple mean of the axial velocity along the span for several distance from the origin is presented in Table 5. From the results of the mean of the axial velocity, the axial induction factor is calculated according to the equation:

$$\langle a \rangle = \frac{V_\infty - \langle C_{z2} \rangle}{V_\infty}$$

An axial induction factor equal to  $a = 0.333$  was set for the design of both wind turbines. The experimental measurements of axial induction factor vary from  $a = 0.339$  at  $z = R_T/3$  to  $a = 0.330$  at  $5R_T/3$  and show low magnitude of variation. Results are really closed to the design settings that proved the good efficiency of the design method.

For comparison, a similar study was conducted with the BWT. Tangential velocity fields (see Fig. 7(b), 7(d)) and profiles (Fig. 7(f)) from the BWT show low magnitude of tangential velocity in the wake of the BWT. The profile for a distance of  $R_T/3$  shows high variation near the root of the blade and is barely explainable. The tangential velocity profiles for various distances show a high degree of similarity. Along the span, the maximum magnitude of tangential velocity is approximately  $1.5 \text{ m.s}^{-1}$ . The measurements of the tangential speed in vortex centers show a decrease from  $1.99 \text{ m.s}^{-1}$  for the first center to  $1.30 \text{ m.s}^{-1}$  for the last one. The distance between each center varies from 82.6 mm to 75.7 mm. Moreover, the distance from the axis of rotation is growing linearly from  $z = 162.6$  mm for the first center to  $z = 179.45$  mm. The wake angle is approximately equal to  $6^\circ$ .

Axial velocity fields and profiles for the BWT are presented in Figs. 8(b), 8(d) and 8(f). Close to the wind turbine, at a distance  $z = R_T/3$ , the axial velocity is approximately constant and equal to  $6 \text{ m.s}^{-1}$ . The associated axial induction factor is  $a = 0.4$ , that is higher than the design axial induction factor. Thus the fluid is more decelerated than predicted by the design specifications. The shapes of axial velocity profiles for the BWT presented in Fig. 8(f) testifies the continuous deceleration of the fluid in the wake of the BWT. As the distance  $z$  from the wind turbine increases, the shape of the axial velocity profiles becomes linear and for a given radial coordinate  $r$ , the axial velocity decreases. At  $r = 2R_T/3$ , the axial velocity decreases from  $6 \text{ m.s}^{-1}$  for  $z = R_T/3$  to  $4 \text{ m.s}^{-1}$  for  $z = 5R_T/3$ . On the contrary, for the same radial coordinate  $r = 2R_T/3$  the axial velocity behind the EWT is approximately constant for various distance  $z$ .

The comparison of the wake angle show that the wake expansion is more significant with the BWT than with the EWT. Moreover, the EWT presents a highly stable wake compared to the BWT. Indeed, the full wake behind the EWT presents an approximately constant axial velocity whereas the wake induced by the BWT is not evenly decelerated. As the distance  $z$  increased, the axial velocity profiles behind the BWT become linear and the deceleration of the fluid is spread to the full wake. It could be explained by the larger negative axial velocity near the hub of the BWT compared to the EWT that induces a higher axial velocity gradient. The results of the stereo-PIV show a satisfying correlation between the design brief of the EWT and the experimental results. In

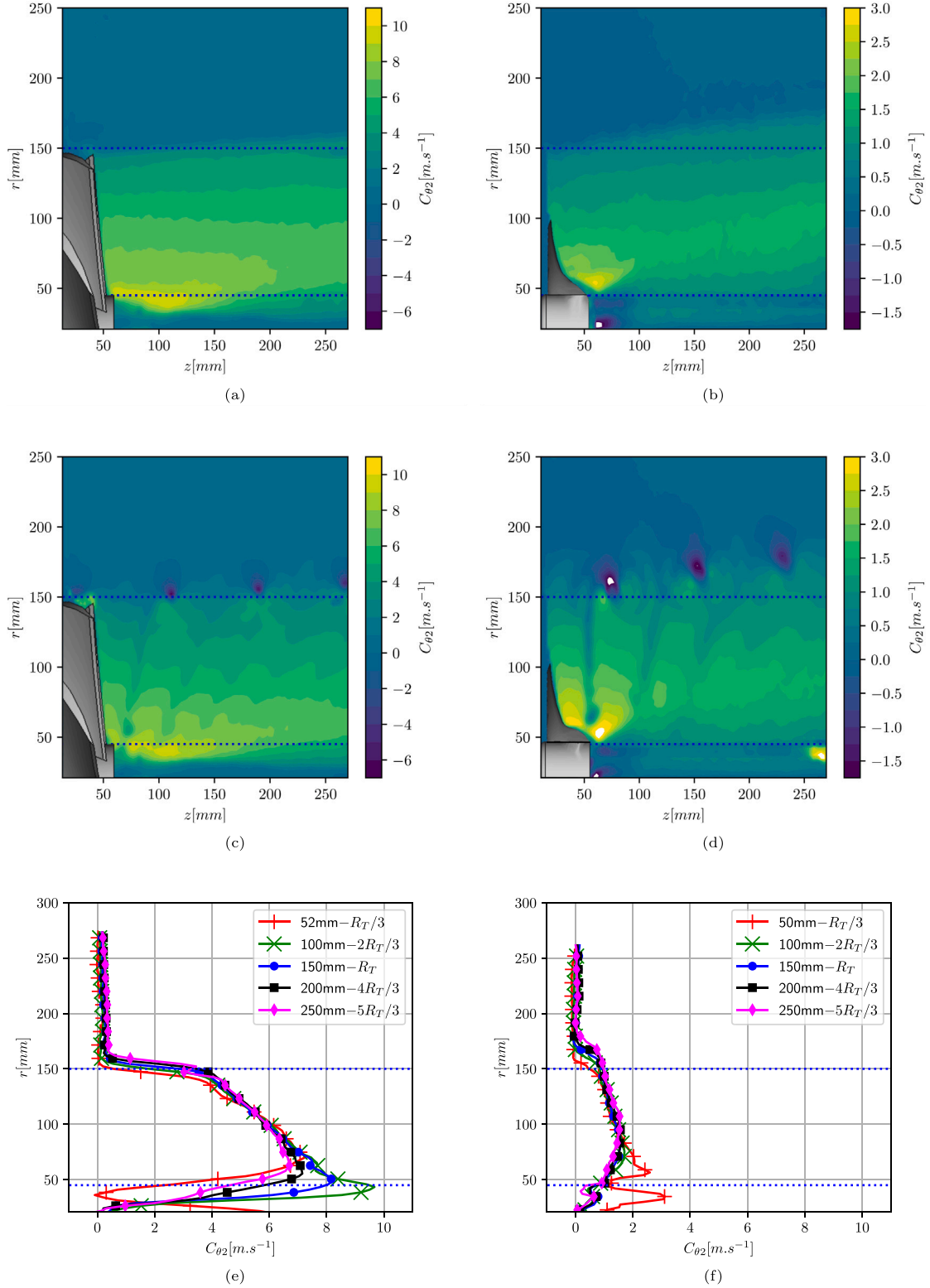


**Fig. 7. Tangential velocity fields and profiles from stereo-PIV acquisitions.** On the left side of the page, the EWT operates at ( $\lambda = 1; V_{\infty} = 10$  m.s<sup>-1</sup>) and on the right side, the BWT at ( $\lambda = 3; V_{\infty} = 10$  m.s<sup>-1</sup>). (7(a), 7(b)): Non-synchronized acquisitions. (7(c), 7(d)): Synchronized acquisitions. (7(e), 7(f)): Tangential velocity profiles derived from non-synchronized acquisitions for various distance  $z$ . Only one marker every five is plotted. The reference frame origin is located at the intersection of the rotation axis with the blade leading edge. Blade span is indicated by (---)

addition, with the same design briefs and a similar mechanical power, not only the EWT induces a higher rotating wake than the BWT – which is consistent with the lower value of the optimal tip-speed ratio – but

also the wake expansion is lower, the slowing down of the fluid is reduced far from the wind turbine and the rotation of the wake persists on a larger distance for the EWT.

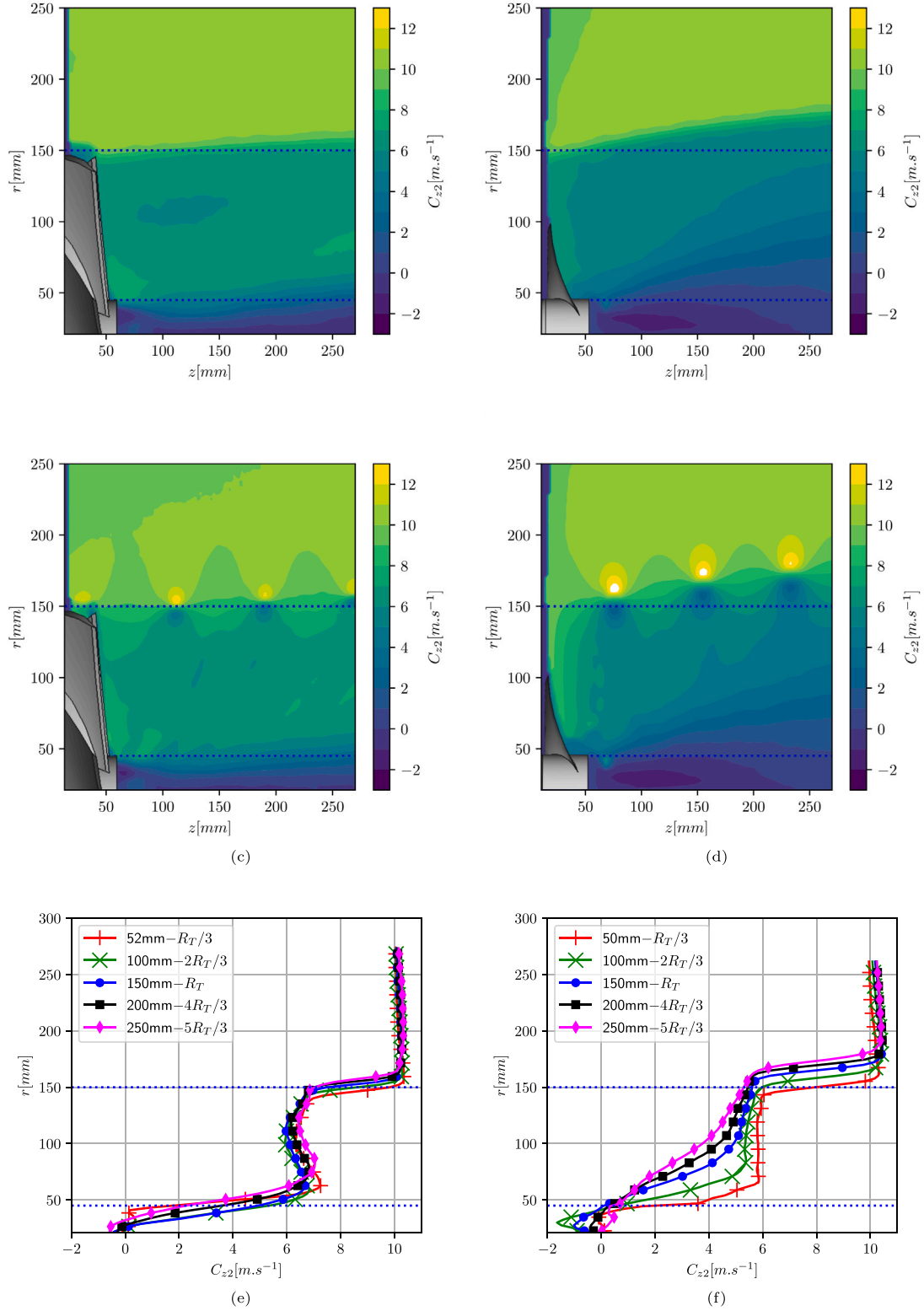


**Fig. 8.** Axial velocity fields and profiles from stereo-PIV acquisitions. On the left side of the page, the EWT operates at ( $\lambda = 1; V_\infty = 10 \text{ m.s}^{-1}$ ) and on the right side, the BWT at ( $\lambda = 3; V_\infty = 10 \text{ m.s}^{-1}$ ). (8(a), 8(b)): Non-synchronized acquisitions. (8(c), 8(d)): Synchronized acquisitions. (8(e), 8(f)): Axial velocity profiles derived from non-synchronized acquisitions for various distance  $z$ . Only one marker every five is plotted. The reference frame origin is located at the intersection of the rotation axis with the blade leading edge. Blade span is indicated by (---)

## 5. Conclusion and perspectives

A 300 mm diameter wind turbine operating at a very low tip-speed ratio  $\lambda = 1$  has been designed with a design method based on the

angular momentum balance coupled to blade cascade deflection in order to follow a prescribed wake vortex law. This wind turbine (EWT) consists of a high solidity blade cascade with 8 blades. It has been tested in wind tunnel and compared to a more classical 3-bladed wind turbine

operating at  $\lambda = 3$  in order to examine its particular behavior. The EWT wind turbine presents a power coefficient similar to the classical wind turbine but at a very low optimum tip-speed ratio. To the author's knowledge, it is the first centimeter-scale wind turbine that achieves such performance at tip-speed ratio  $\lambda = 1$ . The wind turbine presents a very low cut-in wind speed and generates high torque at low tip-speed ratio that makes it an efficient wind turbine for low wind speed applications. Moreover, the EWT presents a monotonous decreasing torque as a function of the angular velocity at constant wind speed. This corresponds to a sensitive response of its angular velocity to a resisting torque control strategy which can be useful for electrical applications.

The wake analysis shows that the wind turbine induces a stable and highly rotating wake, compared to the classical wind turbine, that could be useful to drive a contra-rotating rotor. The absence of vortex breakdown behind the wind turbine is also a source of motivation to keep working on this design method.

However, the proposed design method needs further refinement and parametric study. First, the tangential velocity downstream of the rotor is not consistent with the one imposed. This indicates that the fluid does not strictly follow the deflection imposed by the blade geometry. A higher solidity, especially at the tip, may improve the containment of the fluid into the blade cascade geometry. Furthermore, the high solidity imposed in the design method can lead to high interaction between blades. Thus the expected deflection of the fluid imposed by the blade geometry could be impacted by the adverse pressure gradient between the suction side of one blade and the pressure side of the next one. For instance, empirical correlations – that depend on the airfoil profile – are available to correct the expected tangential velocity when the Euler's turbomachinery theorem is applied in the design of pumps and turbines in confined air flow. Unfortunately, few experimental data are available for open air flow. In addition, the present wind turbine has been designed with an arbitrary constant vortex law, in order to unload the blade root towards more external sections of the blade, and without any loss model. It would be interesting to try other load distributions such as the optimum law issued from the Glauert's model for instance which partially includes losses. Finally, once suitable blade cascade deflection correlations come to be established, an estimate of the efficiency should be included in the method in an iterative way. Thus, the perspectives of this work are on the one hand to characterize the deflection of 2D blade cascades, and on the other hand to perform a parametric investigation of the effects of parameters such as the number of blades, the blade cascade solidity or the hub ratio, and studies of the effects of the vortex distribution on the performance and the wake of such wind turbines.

#### Declaration of competing interest

The authors declare that they have no known competing financial interests or personal relationships that could have appeared to influence the work reported in this paper.

#### References

- Abhishiktha Tummalala, Ratna Kishore Velamati, Dipankur Kumar Sinha, V. Indraj, V. Hari Krishna, A review on small scale wind turbines, *Renew. Sustain. Energy Rev.* 56 (2016) 1351–1371.
- Ravi Anant Kishore, Shashank Priya, Design and experimental verification of a high efficiency small wind energy portable turbine (SWEPT), *J. Wind Eng. Ind. Aerodyn.* 118 (2013) 12–19.
- H. Glauert, Airplane propellers, in: *Aerodynamic Theory: A General Review of Progress under a Grant of the Guggenheim Fund for the Promotion of Aeronautics*, Springer Berlin Heidelberg, Berlin, Heidelberg, 1935.
- Jens Nørkær Sørensen, General Momentum Theory for Horizontal Axis Wind Turbines, in: *Research Topics in Wind Energy*, Vol. 4, Springer International Publishing, Cham, 2016.
- A. Betz, *Windenergie und ihre Ausnützung durch Windmühlen*, Vandenhoeck and Ruprecht, Göttingen, 1926.
- Tony Burton, David Sharpe, Nick Jenkins, Ervin Bossanyi, *Wind Energy Handbook*, 2002.
- N.E. Joukowsky, Vortex theory of a rowing screw, in: *Trudy Otdeleniya Fizicheskikh Nauk Obshchestva Lubitelei Estestvoznaniya*, Vol. 16(1), 1912.
- D.H. Wood, Maximum wind turbine performance at low tip speed ratio, *J. Renew. Sustain. Energy* 7 (5) (2015) 053126.
- Jorge Elizondo, Jaime Martínez, Oliver Probst, Experimental study of a small wind turbine for low- and medium-wind regimes, *Int. J. Energy Res.* 33 (3) (2009) 309–326.
- Maryam Refan, Horia Hangan, Aerodynamic performance of a small horizontal axis wind turbine, *J. Sol. Energy Eng.* 134 (021013) (2012).
- Ronit K. Singh, M. Rafiuddin Ahmed, Blade design and performance testing of a small wind turbine rotor for low wind speed applications, *Renew. Energy* 50 (2013) 812–819.
- João P. Monteiro, Miguel R. Silvestre, Hugh Piggott, Jorge C. André, Wind tunnel testing of a horizontal axis wind turbine rotor and comparison with simulations from two blade element momentum codes, *J. Wind Eng. Ind. Aerodyn.* 123 (2013) 99–106.
- Meng-Hsien Lee, Y.C. Shiah, Chi-Jeng Bai, Experiments and numerical simulations of the rotor-blade performance for a small-scale horizontal axis wind turbine, *J. Wind Eng. Ind. Aerodyn.* 149 (2016) 17–29.
- Salih N. Akour, Mohammed Al-Heydari, Talha Ahmed, Kamel Ali Khalil, Experimental and theoretical investigation of micro wind turbine for low wind speed regions, *Renew. Energy* 116 (2018) 215–223.
- Ali M. Abdelsalam, W.A. El-Askary, M.A. Kotb, I.M. Sakr, Experimental study on small scale horizontal axis wind turbine of analytically-optimized blade with linearized chord twist angle profile, *Energy* 216 (2021) 119304.
- Yasuyuki Nishi, Yusuke Yamashita, Terumi Inagaki, Study on the rotor design method for a small propeller-type wind turbine, *J. Therm. Stresses* 25 (4) (2016) 355–362.
- Hiroyuki Hirahara, M. Zakir Hossain, Masaaki Kawahashi, Yoshitami Nonomura, Testing basic performance of a very small wind turbine designed for multi-purposes, *Renew. Energy* 30 (8) (2005) 1279–1297.
- Ravi Anant Kishore, Anthony Marin, Shashank Priya, Efficient direct-drive small-scale low-speed wind Turbine, *Energy Harvest. Syst.* 1 (1–2) (2014) 27–43.
- Fabio Mendonca, Joaquim Azevedo, Design and power production of small-scale wind turbines, in: *2017 International Conference in Energy and Sustainability in Small Developing Economies (ES2DE)*, IEEE, Funchal, Portugal, 2017, pp. 1–6, <http://ieeexplore.ieee.org/document/8015331/>.
- Yung-Jeh Chu, Heung-Fai Lam, Comparative study of the performances of a bio-inspired flexible-bladed wind turbine and a rigid-bladed wind turbine in centimeter-scale, *Energy* 213 (2020) 118835.
- Fujun Xu, Fuh-Gwo Yuan, Lei Liu, Jingzhen Hu, Yiping Qiu, Performance prediction and demonstration of a miniature horizontal axis wind turbine, *J. Energy Eng.* 139 (3) (2013) 143–152.
- David Rancourt, Ahmadreza Tabesh, Luc Fréchette, Evaluation of centimeter-scale micro wind mills: Aerodynamics and electromagnetic power generation, *Proc. PowerMEMS* (2007) 93–96.
- M. Perez, S. Boisseau, P. Gasnier, J. Willemin, M. Geisler, J.L. Reboud, A cm scale electret-based electrostatic wind turbine for low-speed energy harvesting applications, *Smart Mater. Struct.* 25 (4) (2016) 045015, Publisher: IOP Publishing.
- Mohamed Y. Zakaria, Daniel A. Pereira, Muhammad R. Hajj, Experimental investigation and performance modeling of centimeter-scale micro-wind turbine energy harvesters, *J. Wind Eng. Ind. Aerodyn.* 147 (2015) 58–65.
- D.A. Howey, A. Bansal, A.S. Holmes, Design and performance of a centimeter-scale shrouded wind turbine for energy harvesting, *Smart Mater. Struct.* 20 (8) (2011) 085021.
- P. Giguère, M.S. Selig, New airfoils for small horizontal axis wind turbines, *J. Sol. Energy Eng.* 120 (2) (1998) 108–114.
- Haseeb Shah, Jasir Kitaba, Sathyajith Mathew, Chee Lim, Experimental Flow Visualization over a Two-Dimensional Airfoil at Low Reynolds Number, 2014.
- Philippe Giguère, Michael S. Selig, Low Reynolds number airfoils for small horizontal axis wind turbines, *Wind Eng.* 21 (6) (1997) 367–380.
- P.B.S. Lissaman, Low-Reynolds-number airfoils, *Annu. Rev. Fluid Mech.* 15 (1) (1983) 223–239.
- D.J. Sharpe, A general momentum theory applied to an energy-extracting actuator disc, *Wind Energy* 7 (3) (2004) 177–188.
- Dennis Leung, Y. Deng, Michael K.H. Leung, Design optimization of a cost-effective micro wind turbine, in: *WCE 2010 - World Congress on Engineering 2010*, Vol. 2, pp. 988–993.
- Matthew M. Duquette, Jessica Swanson, Kenneth D. Visser, Solidity and blade number effects on a fixed pitch, 50 W horizontal axis wind turbine, *Wind Eng.* 27 (4) (2003) 299–316.
- M.S. Selig, Summary of Low Speed Airfoil Data, in: *Summary of Low Speed Airfoil Data*, (Vol. 2) SoarTech Publications, 1995.
- S.L. Dixon, C.A. Hall, Two-dimensional cascades, in: S.L. Dixon, C.A. Hall (Eds.), *Fluid Mechanics and Thermodynamics of Turbomachinery*, sixth ed., Butterworth-Heinemann, Boston, 2010, pp. 53–96, (Chapter 3).
- M. Raffel, Christian Willert, Juergen Kompenhans, *Particle Image Velocimetry: A Practical Guide*, 1998.